Terahertz optical thickness and birefringence measurement for thermal barrier coating defect location

ANDREW J. WADDIE,[1] PETER J. SCHEMMEL,[1,2] CHRISTINE CHALK,[3] LUIS ISERN,[3] JOHN R. NICHOLLS,[3] AND ANDREW J. MOORE[1,*]

[1]*Institute of Photonics and Quantum Sciences, Heriot-Watt University, Edinburgh EH14 4AS, UK*
[2]*Current address: NASA Glenn Research Center, Cleveland, OH 44135, USA*
[3]*Surface Engineering Precision Institute, Cranfield University, Cranfield, Bedfordshire MK43 0AL, UK*
[*]*a.moore@hw.ac.uk*

Abstract: We present a normal incidence terahertz reflectivity technique to determine the optical thickness and birefringence of yttria-stabilized zirconia (YSZ) thermal barrier coatings (TBCs). Initial verification of the method was achieved by measurement of a set of fused silica calibration samples with known thicknesses and showed excellent agreement (<1% of refractive index) with the literature. The THz-measured optical thickness and its variation through the depth profile of the YSZ coating are shown to be in good agreement (<4%) with scanning electron microscope cross-sectional thickness measurements. In addition, the position of discontinuities in both the optical thickness and birefringence appear to be correlated to coating failure points observed during accelerated aging trials.

1. Introduction

Current generation gas turbine jet engines produce optimally efficient thrust when the combustion chamber gas flows are maintained at high (~1300-1500 °C) temperatures. These temperatures are above the melting point of the metallic superalloys used in the fabrication of the individual constituent parts of the gas turbine combustion chambers. Thermal management to avoid melting consists of two parts – forced air cooling, where the part of the combustion chamber airflow not required for fuel-air mixing is used to cool the metallic surfaces; and thermal barrier coatings, which limit the heat flow to the metallic surfaces without the addition of significant thickness and weight to the combustion chamber. Yttria-stabilized zirconia (YSZ) thermal barrier coatings (TBCs) have been shown [1] to possess sufficiently low thermal conductivity and, when combined with forced air cooling, can reduce the metallic surface temperature by ~100-150 °C – i.e. below the melting point of the superalloy. The trend towards higher combustion chamber operating temperatures, and, hence, improved gas turbine efficiencies has shown no sign of abating with a predicted increase of ~10 °C/year to greater than 1750 °C in the near future [2].

The non-destructive measurement of TBC material parameters, and their evolution with aging, is of critical importance to their deployment and in-service monitoring. A range of different contact-type methods [3–5] have been used to provide this information. The applicability of contact methods is limited by the need for good physical contact with the coated surface and therefore the development of non-contact optical methods has also been necessary. THz time-domain spectroscopy (TDS) [6–10] enables either the thickness or the refractive index of the coating to be determined by measuring the time delay of an ultrashort pulse (~500 fs – 2 ps duration) through the sample. THz illumination is preferred because TBCs are opaque at visible optical frequencies and GHz illumination does not provide adequate resolution for the

thin coatings. References [6] and [8] study a number of different materials and structures while references [7], [9] and [10] are more focused on the particular combination of materials and structures used in thermal barrier coatings, i.e. YSZ coatings on metallic substrates. Reference [8] uses refractive indices from the literature to determine the sample thicknesses and shows large relative errors (up to 68%) when compared to the physically measured thicknesses. In [7] and [9], the mean refractive index of YSZ is determined using a sample of known thickness and this value is then used to determine the refractive index [7] or thickness [9] of further coatings (ranging from 300 μm to 700 μm) with relative errors of 3-9% [7] and 5% [9] respectively. References [6] and [10] calculate the refractive index from the Fourier transform of the reflected pulses and then determine the thickness of an unknown sample – [6] shows measurement errors in the range 7-22% while [10] shows errors in the range 3-10%.

In this paper, we present an alternative THz optical-thickness technique based on the measurement of the reflectivity of thin-film TBC structures using a relatively high power (5 mW) tunable THz laser. The combination of high power and an intensity normalization procedure produces well-formed thin film reflectivity fringes providing sufficient signal-to-noise ratio that the effects of water absorption lines [11] are minimized. This enables the system to be operated with a relatively long (∼2 m) optical path between the emitter, sample and detector, and without the humidity control that is often required with TDS [10]. The addition of rotation opto-mechanics to the sample mount and a linear analyzer to the beam path also permits the measurement of the retardation (and thus the birefringence) of the sample.

This method is used to determine the coating optical thickness, defined as the refractive index times the physical thickness, to avoid the need for the coating parameter pre-determination. Initial verification of the optical thickness measurement is achieved by means of a set of uncoated and YSZ-coated fused silica (SiO$_2$) samples. The optical thickness measurement method, with the addition of Carré phase stepping to remove the optical thickness ambiguity inherent in normal-incidence reflectivity fitting, is then applied to a thermal barrier coating sample. A similar strategy is followed for the birefringence measurement with initial verification of the method being achieved by measurement of a GHz waveplate of known thickness and birefringence before application to a TBC sample. We demonstrate that the position of discontinuities in both the optical thickness and birefringence appear to be correlated to coating failure points observed during accelerated aging trials. The results of these aging trials will be presented in a future publication.

2. Optical thickness and birefringence modelling

The optical thickness is determined by fitting a thin film model, which can include multiple layers and surface roughness, to the measured reflectivity spectrum across a range of THz frequencies. The birefringence measurement matches the measured intensity variation of the reflected illumination as a function of the sample angle to a simple theoretical polarization model of the THz measurement system.

2.1. Optical thickness

The two main optical modelling methods used to calculate reflection and transmission characteristics of thin films are the Transfer Matrix Method (TMM) [12], which gives the reflectivity and transmissivity simultaneously, and Rouard's Method [13], which requires a separate implementation for each. Both methods have similar accuracy although the TMM requires greater computation time. For the relatively small number of frequencies in the measurements presented in this paper, this additional computational overhead is negligible and so the TMM was chosen because of its flexibility for including additional layers.

The multilayer thin film structure typical of TBCs is defined by a number (N) of layers each specified by a complex refractive index ($\tilde{n}_a = n_a + ik_a$) and a thickness (t_a), that is embedded

between two infinite thickness layers specified by the indices 0 (top) and N+1 (bottom). The transfer matrix, which details the amplitudes of the forward and backward propagating waves in the top and bottom infinite layers, is expressed by a sequence of 2×2 Fresnel coefficient (F_a) and propagation (P_a) matrices. In order to account for the scattering due to the surface roughness of each layer in the thin-film structure, an extra scattering matrix (S_a) is added to the basic TMM with the arithmetical mean deviation of the surface (r_a), being used to determine the overall scattering strength (σ_a) [14]. The surface roughness term assumes that Kirchoff's approximation holds for the TBC structures, i.e. the overall height variation of the surface is much less than the wavelength of the THz illumination and the lateral dimensions of the roughness are slightly below or comparable to the wavelength of the THz illumination.

$$
\begin{bmatrix} M_{11} & M_{12} \\ M_{21} & M_{22} \end{bmatrix} = \left[\prod_{a=1}^{N} F_a S_a P_a \right] F_{N+1}
$$
$$
= \left[\prod_{a=1}^{N} \begin{bmatrix} 1/\tau_a & \rho_a/\tau_a \\ \rho_a/\tau_a & 1/\tau_a \end{bmatrix} \begin{bmatrix} e^{-\sigma_a^2} & 0 \\ 0 & e^{-\sigma_a^2} \end{bmatrix} \begin{bmatrix} e^{-i\delta_a} & 0 \\ 0 & e^{i\delta_a} \end{bmatrix} \right] F_{N+1}
$$

(1)

where $\delta_a = \frac{2\pi \tilde{n}_a t_a}{\lambda}$; $\rho_a = \frac{(\tilde{n}_{a-1} - \tilde{n}_a)}{(\tilde{n}_{a-1} + \tilde{n}_a)}$; $\tau_a = \frac{(2\tilde{n}_{a-1})}{(\tilde{n}_{a-1} + \tilde{n}_a)}$; *and* $\sigma_a = \frac{4\pi r_a \tilde{n}_a}{\lambda}$.

The amplitude reflection (r) of the structure is calculated from the transmission matrix by comparing the upward-travelling top surface wave (M_{21}) to the downward-travelling top surface wave (M_{11}). The reflectivity (R) of the structure is then calculated by multiplying the amplitude reflection by its complex conjugate.

$$
R = rr^* = \left[\frac{M_{21}}{M_{11}} \right] \left[\frac{M_{21}}{M_{11}} \right]^*
$$

(2)

The physical structures of the fitting models used for the method verification and the thermal barrier coating samples in this paper are shown in Fig. 1.
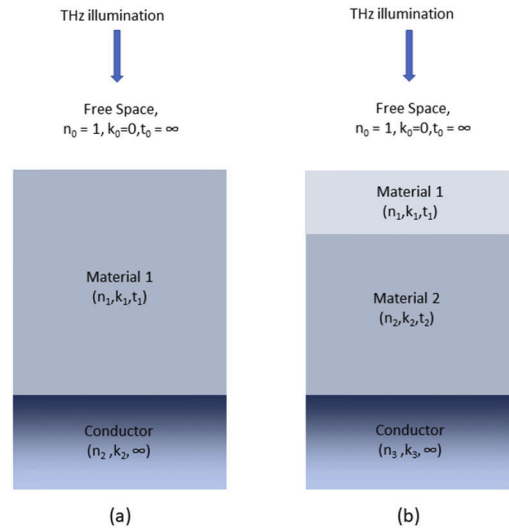

Fig. 1. Thin film model configurations and parameters. (a) Single layer (b) Two-layer.

The simplest model structure consists of a single uniform layer of material embedded between two infinite thickness layers of free space for the top (incident) layer and a conductor for the metal

substrate on which the coating is deposited. The transmission matrix for the single layer model is:

$$M_1 = F_1 P_1 F_2 = \frac{1}{\tau_1} \begin{bmatrix} 1 & \rho_1 \\ \rho_1 & 1 \end{bmatrix} \begin{bmatrix} e^{-i\delta_1} & 0 \\ 0 & e^{i\delta_1} \end{bmatrix} \begin{bmatrix} 1 & \rho_2 \\ \rho_2 & 1 \end{bmatrix} \frac{1}{\tau_2}$$

$$\frac{1}{\tau_1 \tau_2} \begin{bmatrix} e^{-i\delta_1} + \rho_1 \rho_2 e^{i\delta_1} & \rho_1 e^{-i\delta_1} + \rho_2 e^{i\delta_1} \\ \rho_1 e^{-i\delta_1} + \rho_2 e^{i\delta_1} & \rho_1 \rho_2 e^{-i\delta_1} + e^{i\delta_1} \end{bmatrix} \tag{3}$$

with the reflectivity of the single layer model given by,

$$R = \frac{\rho_1^2 + \rho_2^2 + 2\rho_1 \rho_2 \cos 2\delta_1}{1 + \rho_1^2 \rho_2^2 + 2\rho_1 \rho_2 \cos 2\delta_1} \tag{4}$$

The surface roughness matrix term was set equal to unity in Eq. (3) to simplify the expression and to emphasize the sinusoidal nature of the reflectivity with the optical phase, δ. The transmission matrix for the two-layer model is developed in an identical way to the single layer model with the addition of the transmission and propagation matrices for layer 2:

$$M_2 = \frac{1}{\tau_1 \tau_2 \tau_3} \begin{bmatrix} 1 & \rho_1 \\ \rho_1 & 1 \end{bmatrix} \begin{bmatrix} e^{-i\delta_1} & 0 \\ 0 & e^{i\delta_1} \end{bmatrix} \begin{bmatrix} 1 & \rho_2 \\ \rho_2 & 1 \end{bmatrix} \begin{bmatrix} e^{-i\delta_2} & 0 \\ 0 & e^{i\delta_2} \end{bmatrix} \begin{bmatrix} 1 & \rho_3 \\ \rho_3 & 1 \end{bmatrix} \tag{5}$$

resulting in a reflectivity with the same general form as the single layer (being the division of two offset sinusoidal functions) but of increased complexity.

2.2. Birefringence

Thermal barrier coatings have been shown to exhibit some degree of birefringence [15]. Both strain-related birefringence, due to the intrinsic strain of the TBC structure, as well as form birefringence, due to the change in the microscopic columnar shape of coating across the deposition surface, are present. The separation of these two sources of birefringence would require a microscopic analysis of the TBC structure and lies outside the scope of this paper. However, a measurement of the magnitude and orientation of the total retardation (φ), and hence the birefringence, can be achieved by in-plane rotation under vertically polarized THz illumination with a fixed 60° to vertical analyzer placed in the beam path after the sample [16]. The reflected intensity variation with rotation angle (θ) is shown in Eq. (6) and was derived from the formulation of [16] with modifications owing to the thin film nature of the samples leading to different sample reflectivities in the vertical (R_v) and horizontal (R_h) polarizations.

$$I = \frac{E_0^2}{4} \left[1 + \sin^2 \frac{\phi}{2} \left[\frac{3R_v^2 - R_h^2}{R_h^2} \right] \sin^2 2\theta + \frac{2\sqrt{3}R_v R_h}{R_v^2} \sin 2\theta \cos 2\theta \right] \tag{6}$$

The retardation is calculated from the minimum and maximum intensity values by

$$\phi = 2\sin^{-1} \sqrt{\frac{(I_{max} - I_{min})}{\left(I_{max} + \frac{3R_v^2}{R_h^2} I_{min}\right)}} \tag{7}$$

3. Experimental and measurement considerations

3.1. Experimental setup

The experimental system was set up as shown in Fig. 2. The 1064nm pump laser (M2-ICE) output is converted into two OPO (M2 Firefly) output beams – a frequency selective THz idler

beam and a near-IR signal beam. The OPO produces THz ~30 ns pulses with a linewidth of ~40 GHz at a 50 Hz repetition rate; the average power is 5mW with an elliptical beam shape of 12 mm x 25 mm at the output port. The output is tunable between 1 and 2 THz with the frequency resolution being the linewidth of the THz output. The frequency range of 1.2 to 1.6 THz was chosen for the optical thickness measurements presented in this paper in order to give a well-formed sinusoidal response in the reflectivity for the specimens tested.
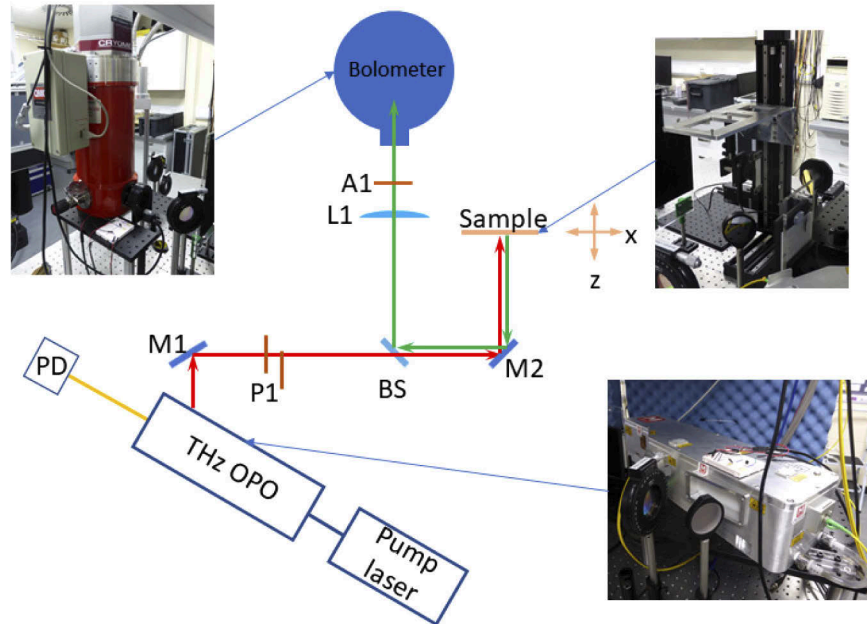

Fig. 2. Schematic of experimental setup. M1 – flat mirror; P1 – linear polarizer; BS – Si beam splitter; M2 – parabolic mirror; L1 – PTFE lens; A1 – linear analyzer; PD – photodiode.

The THz output from the laser is reflected by a flat mirror (M1) and then passed through a linear polarizer (P1) to ensure that the illumination entering the measurement system is vertically polarized. The incident THz beam (shown in red in Fig. 2) is then focused on to the sample by parabolic mirror M2 (reflective focal length = 152.4 mm), to produce a near-diffraction limited spot size of ~0.5 mm x 1.0 mm. The reflected beam (shown in green in Fig. 2) is then transmitted back along the incident beam path and reflected by the Si beam splitter (BS) into the detection arm of the instrument. PTFE lens L1 (effective focal length = 100 mm) is used to focus the reflected THz beam onto the single-pixel cyrostatically-cooled superconducting bolometer (QMC Instruments Ltd QNbTES/X). The propagation distance of the THz beam is 0.7 m from laser to sample and 1.0 m from sample to detector. Lens L1 was chosen over a parabolic mirror simply to keep the overall path length down for the optical bench used. For the birefringence measurements only, a linear analyzer (A1) was placed between the PTFE lens and the bolometer. The bolometer is a highly sensitive instrument (NEP < 2 pW/Hz$^{1/2}$), but the Firefly THz source is sufficiently bright that a less sensitive detector, such as a room-temperature pyrometer, could be used without any change to either the experimental system or the data analysis for the TBC samples studied in this paper.

The sample can be translated in X, Y and Z by means of a set of motorized translation stages (Zaber Technologies Inc. X-LRQxxxBL-E01; x-,y- 450 mm; z- 75 mm). The acceleration and movement speed of the translation stages were set to ensure that the samples were completely

stationary before each THz measurement was taken. The sample is mounted on a motorized rotation stage so that it can rotate about the Z-axis in the XY plane for birefringence measurements, i.e. the THz incidence angle will remain normal throughout the rotation operation.

The output from the pump laser exhibited a pulse-to-pulse intensity variation and, in order to compensate for this, the near-IR signal beam was monitored by an InGaAs photodiode PD (Thorlabs DET04CFC/M) and used to normalize the bolometer measurement. In addition, each measurement point was averaged over 50 pulses to improve the SNR of the data. The sensitivity of the bolometer is such that any noise observed in the measurements was entirely due to pulse-to-pulse intensity variation of the laser source rather than the detector. The slow sample translation speed, combined with the pulse averaging and low repetition rate of the THz source, resulted in a relatively slow overall measurement speed - approximately 1.5 seconds per translation and 1 second per measurement frequency.

3.2.　*Measurements and samples*

The optical thickness measurements involved recording a reflectivity spectrum for each specimen, i.e. measuring the reflected intensity as the optical phase δ was varied by tuning the frequency of the THz emission. Measurements were made at a number of points uniformly distributed across the sample by moving it on the XY stages. The birefringence measurements involved recording the variation in reflected intensity (with the analyzer A1 in position) as the sample was rotated in its own plane on the rotation stage. Birefringence measurements were also measured at a number of points distributed across the sample and, for those measurement points not on the rotation axis of the rotation stage, a positional correction with the XY stages was applied at each measurement angle to maintain the same point in the focused THz spot.

The samples were divided into two categories – an initial set of verification samples and a follow-on set of thermal barrier coating samples. The optical thickness verification samples comprised three 1 mm thick fused silica substrates, one with no coating and two coated, using EB-PVD, with YSZ layers of nominal thickness 120 and 240 μm. The birefringence verification sample was a crystalline quartz multi-order quarter-wave plate (Tydex WP-CQ-D50.8-OW909-L/4, thickness=4.83 mm, Δn=0.04705) designed for a wavelength of 909 μm (f = 330 GHz).

The YSZ thermal barrier coating samples were fabricated using electron beam – physical vapor deposition (EB-PVD) on to a metallic superalloy substrate [17,18]. The substrates were initially coated with a 25-40 μm thick β-NiAl adhesion promotion (or bond coat) layer before the nominally 300 μm thick ceramic YSZ coating was deposited. An interstitial layer of Al_2O_3 thermally grown oxide (TGO) arises at the boundary between the bond coat and the YSZ layer during deposition and plays a major role in TBC failure during thermal cycling [3].

4.　**Optical thickness measurements**

4.1.　*Verification samples*

The reflectivity spectra of the three optical thickness verification samples mounted on top of an Al mirror were recorded between 1.2 and 1.6 THz at a single point near the center of each sample (Fig. 3). The recorded spectra have been normalized by a separate intensity measurement recorded directly from the metal substrate, in order to minimize the effects of variations in the source emission and detector response with frequency and the effect of water absorption lines [15]. A fitting process was applied to each spectrum using the single layer model for the uncoated sample and the two-layer model for the two coated samples. The conductor refractive index of Al (= 452 + i 506) [19] was used. The material parameters of each sample (namely n, k and t for each layer) and, hence, the optical thickness, are derived by minimizing the reduced χ2 error between the experimental reflectivity spectrum and the appropriate modelled reflectivity spectrum, (Eq. (2)).
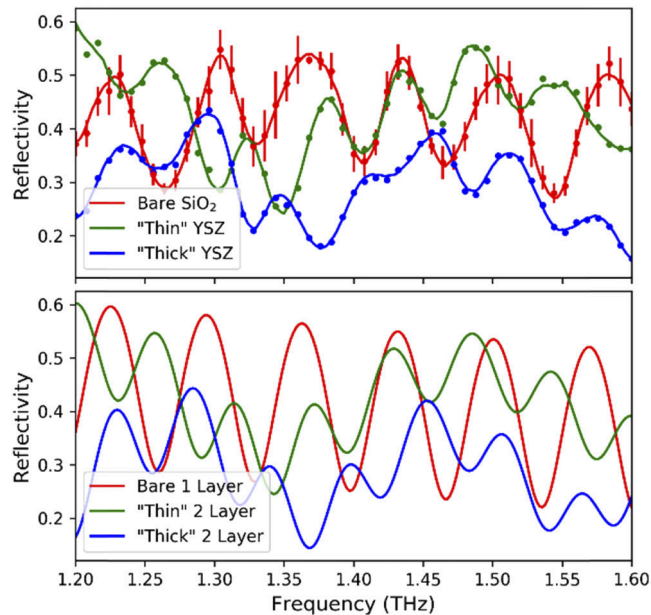
Fig. 3. (Top) Reflectivity spectra for verification samples: Red - uncoated fused silica; Green - thin YSZ coating on fused silica; Blue - thick YSZ coating on fused silica. (Bottom) Minimum reduced χ2 fit for verification samples. For clarity, the error bars for the Thin YSZ and Thick YSZ results in the top graph have been omitted but they are of similar magnitude to those shown for the Bare SiO_2 line.

The choice of error minimization procedure used to search the available parameter space is highly dependent upon the shape of the multi-dimensional error surface and the frequency and depth of global and local minima. The predominantly sinusoidal nature of the reflectivity spectra means that the arbitrary addition of a multiple of π to the optical phase (δ) will tend to produce an equally good fit to the experimental data – any variation will be entirely due to the very small changes in the layer reflection coefficients (ρ). This effect can be seen in Fig. 4 where the reduced χ^2 error of the fit to a modelled set of reflectivity fringes for the one-layer model is shown for a range of different n and t values.

Even in this theoretical example, with no experimental noise, there are several local minima of approximately equal minimum error: they preclude the use of a conventional gradient descent algorithm for the error minimization because the final result will be highly dependent on the initial starting point. The Simulated Annealing error minimization algorithm has been shown to be relatively robust in the presence of this type of local minima [20]. This algorithm is a stochastic walk through the available parameter space, where the probability of an increase in the minimization error being accepted is a function of the change in minimization error and a so-called annealing temperature. The cost function used for the annealing step acceptance is the mean square error between the intensity of the experimental reflectivity fringes and the modelled fringes defined by Eqs. (1)–(5). As the minimization progresses, the annealing temperature is gradually reduced until only decreases in the minimization error are accepted. As there is still a finite probability of the minimization landing in one of the local minima, a statistically significant number of fitting runs (>1000) are performed, with each individual fitting run for a single point taking ~0.3 seconds using a non-optimized Python code running on a 3GHz general purpose PC. The final selection of the "correct" set of material parameters is then made from the distribution of the results. The distribution for 5000 fitting runs on the reflectivity spectrum of the "thin"
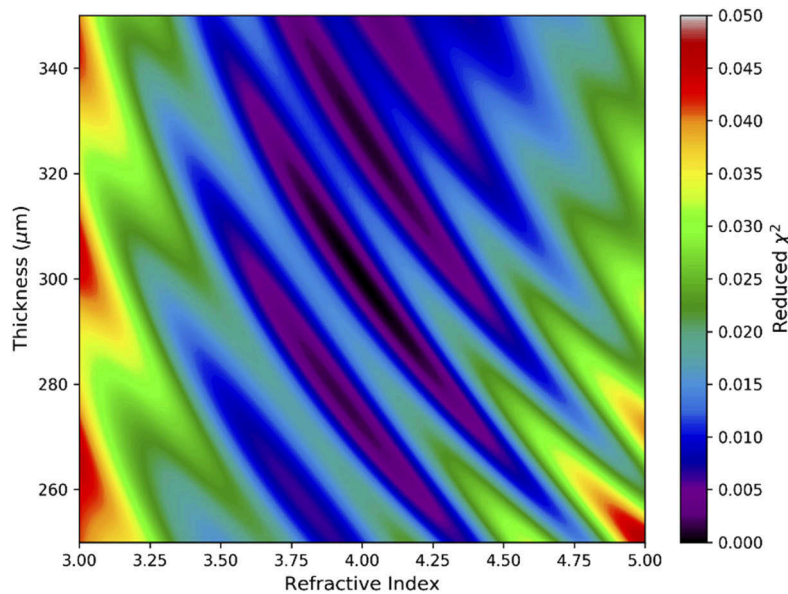
Fig. 4. Reduced χ^2 error surface for fit to single layer model showing set of local minima around the global minimum at the center of the figure.

coated verification sample (from Fig. 3) is shown in Fig. 5 where there is a clear minimum error n*t "band" lying just above n*t=2,600.
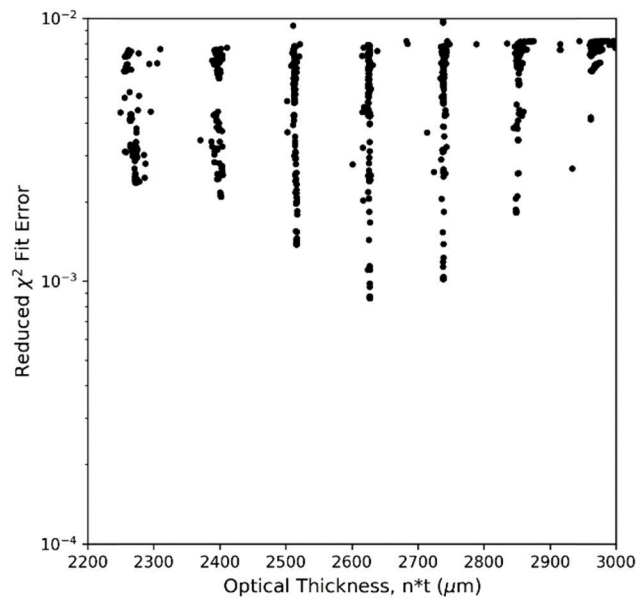

Fig. 5. Variation of mean square fitting error for 5000 fitting runs for "thin" coated fused silica verification sample.

The fitted reflectivity spectra for each of the verification samples are shown in Fig. 3. In each case, there was a clear minimum error "band" in optical thickness from the fitting procedure. The frequency of the modelled sinusoid for the single-layer sample, and the beating sinusoids for

the two-layer samples, are a good match for the experimental data, which is directly related to the combined optical thickness of the layers. There is some deviation between the modelled and experimental minima/maxima that is most likely due to extraneous absorption in the samples, such as material non-uniformities, which is not considered by the transfer matrix model used in this paper. The physically measured thickness of the uncoated fused silica sample was used to determine its refractive index from the single layer model. Comparison with the literature [21,22] shows agreement to the real refractive index to within 1% (1.977 measured here, compared to 1.975 in [21]) and to within 2% to the imaginary refractive index (7.73×10^{-3}, compared to 7.87×10^{-3} in [21]). The known optical thickness of the substrate and the refractive index of YSZ were used to determine the coating thickness on the two coated SiO2 verification samples from the two-layer model. The physical coating thicknesses were measured by using an optical microscope and were determined to be 143.2 μm ("thin") and 238.8 μm ("thick") – the estimated thicknesses from the THz measurements were 138.9 μm and 247.6 μm respectively, i.e. the fitted and physically measured coating thicknesses agreed to within 5%.

4.2. Thermal barrier coating

The reflectivity spectrum of the TBC sample was recorded between 1.2 and 1.6 THz for a 3×9 grid of measurement points on a 7mm grid spacing resulting in a total measurement time of 70 minutes. Figure 6 shows the results from the reflectivity measurements and n*t fits at two points from the 3×9 set, one close to the center of the sample and the other towards the bottom. The frequency range used for the fit was restricted to 1.25-1.35 THz to avoid the need for a coating dispersion model describing the variation of the complex refractive indices with wavelength. The infinite thickness conductor in the model is the bond coat with a complex refractive index, n=298 + i379, calculated using the refractive indices of the constituent metals [19,23] in the appropriate proportions for the β-NiAl bond coat.

Figure 6(a) shows the n*t bands recovered from the Simulated Annealing error minimization procedure. The center point represents a typical measurement: it shows a global minimum (at n*t = 1141.3 μm) although the minimum error of the adjacent n*t band is much closer to the global minimum than was the case for Fig. 4. The resolution of the fit is estimated to be 2%, based on the standard deviation of ~22 μm for the points about the mean n*t value of 1141.3 μm of the band. The bottom point measurement in Fig. 6(a) represents ~20% of points in each data set for which there was no distinct global minimum. In this case there are three different n*t bands which might be considered to contain the global minimum. This uncertainty in the correct n*t band did not occur in the validation samples but arose at some points in the TBC measurement because of reduced signal-to-noise in the reflectivity spectra due to increased absorption, and because of dispersion in the coating material. The effect of dispersion can be seen in Fig. 6(b), where the period of the reflectivity fringes gradually increases at higher frequencies.

The indeterminacy in the n*t band for this small number of points was resolved by an ancillary full-field optical thickness measurement. The reflectivity was measured at a greater spatial resolution (a 1 mm x 1 mm grid spacing with a total measurement time of ~250 minutes) but at four frequencies only, to produce the reflectivity maps shown in Fig. 7(a). The start frequency was chosen as the fringe minima closest to the center of the measured frequency range and the frequency step as half the frequency between that minimum and the adjacent higher frequency maximum. These four chosen frequencies, with a linear phase step of ~π/2, are indicated by large crosses in Fig. 6(b). The intensity in each image was scaled, to convert the reflectivity intensity into a standard two-beam interferogram intensity, and the optical phase at each point was calculated using the Carré phase stepping algorithm [24] (Fig. 7(b)). The modulo 2π wrapped phase was unwrapped using a 2D reliability unwrapping algorithm [25].

Figure 8(a) shows the unwrapped phase, onto which the 3×9 grid of n*t measurements from the fits to the reflectivity spectra have been superimposed, converted into optical phase δ as
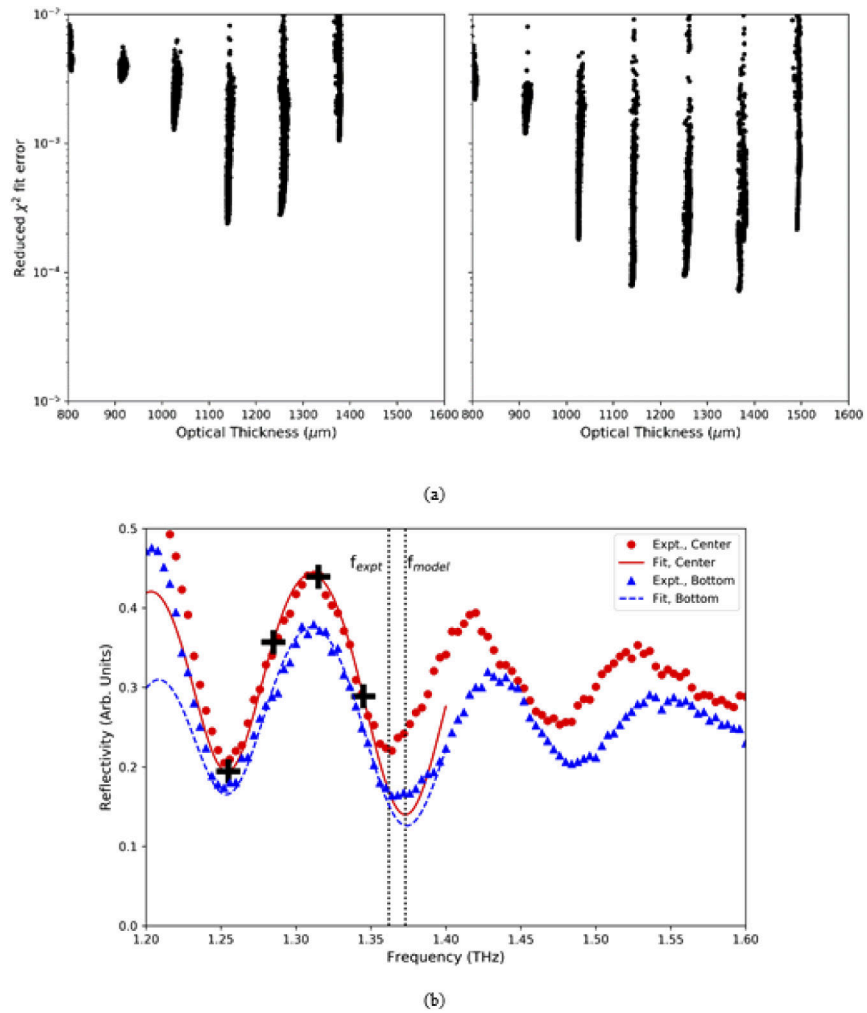
Fig. 6. (a) Reduced χ^2 fit error for YSZ thermal barrier coating on β-NiAl bond coat at center (L) and bottom (R) of sample. (b) Experimental (points) and fitted (lines) reflectivity spectra of YSZ thermal barrier coating at center and bottom of sample.
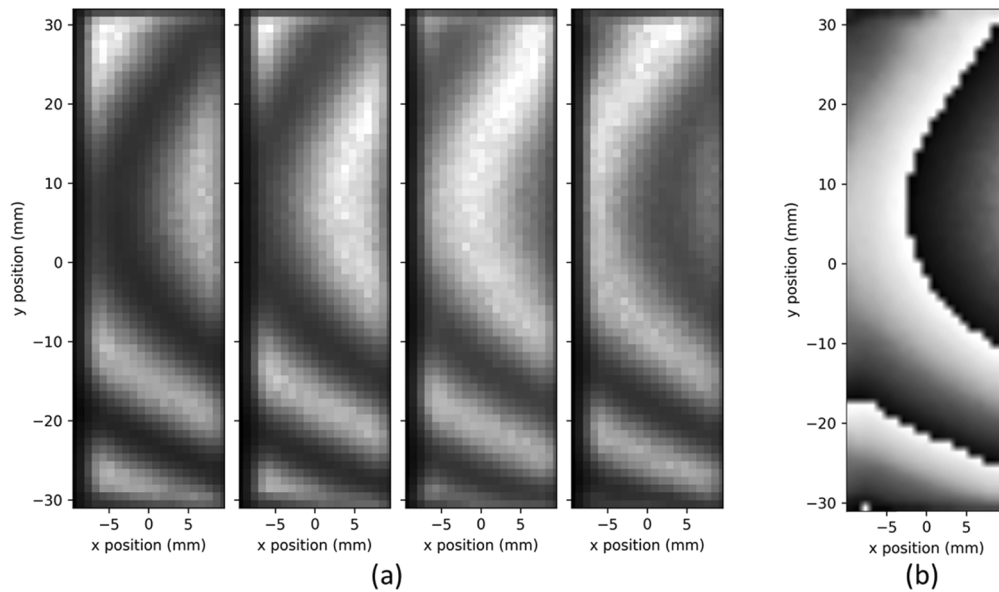
Fig. 7. Results from phase stepping measurement on YSZ-coated sample. (a) Reflectivity images at four discrete frequencies (from left to right – 1.255, 1.285, 1.315 and 1.345 THz). (b) Wrapped full-field phase.

defined by Eq. (1), at a frequency corresponding to the mean of the four frequencies used in the phase stepping (in this case, 1.3 THz). The two approaches are complementary: the full field unwrapped phase represents the relative thickness variation over the field of view, while the n*t fit measurements represent the absolute thickness at independent points albeit with an uncertainty at a small number of points due to no clear minimum from the Simulated Annealing fitting procedure. It is straightforward to add multiples of 2π to the entire full-field unwrapped phase map until the best fit to the majority of fitted spectra points is found, and then making local
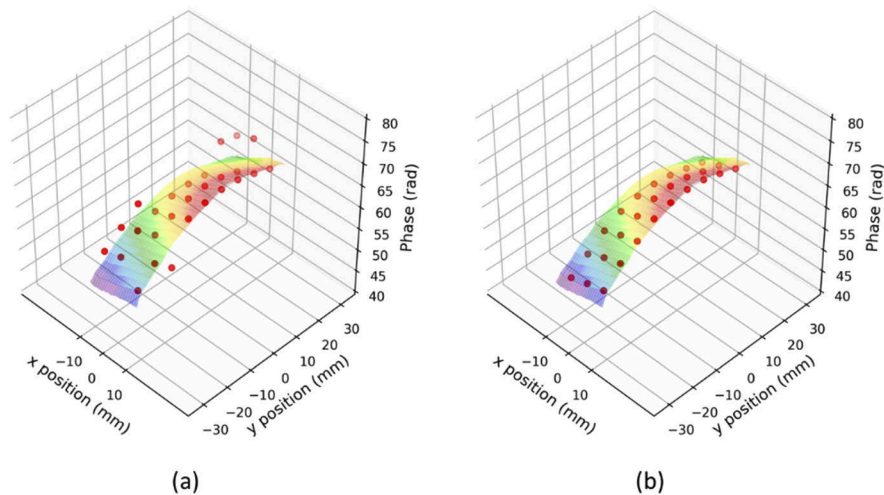

Fig. 8. Full field phase and n*t fitting matching. Comparison between unwrapped full-field phase and n*t fitting phase before (a) and after (b) piston and local phase correction.

π adjustments to the outliers, corresponding to a shift between the optical thickness bands of Fig. 6(a), to achieve the final result, Fig. 8(b). The overall thickness variation of the TBC is roughly spherical due to the spherically expanding vapor plume produced by the source ingot in the coating chamber.

The matched optical thickness phase is converted back into an optical thickness to permit direct comparison with the measured physical thickness of the TBC, which was determined by destructive sectioning of the sample followed by SEM measurement of the vertically mounted sections (Fig. 9). The figure shows the bond layer with the TBC above it. The thin black line between the two is the thermally grown oxide layer that was mentioned in the Introduction. The TBC itself has two distinct regions: a region of small and randomly orientated equiaxed grains that form close to the bond layer at the start of deposition; and a columnar region of large columns with specific crystal orientations that form later in the deposition. The single layer model was used to consider the TBC as a single structure and the two-layer model was used to estimate the thickness of the columnar and equiaxed zones.
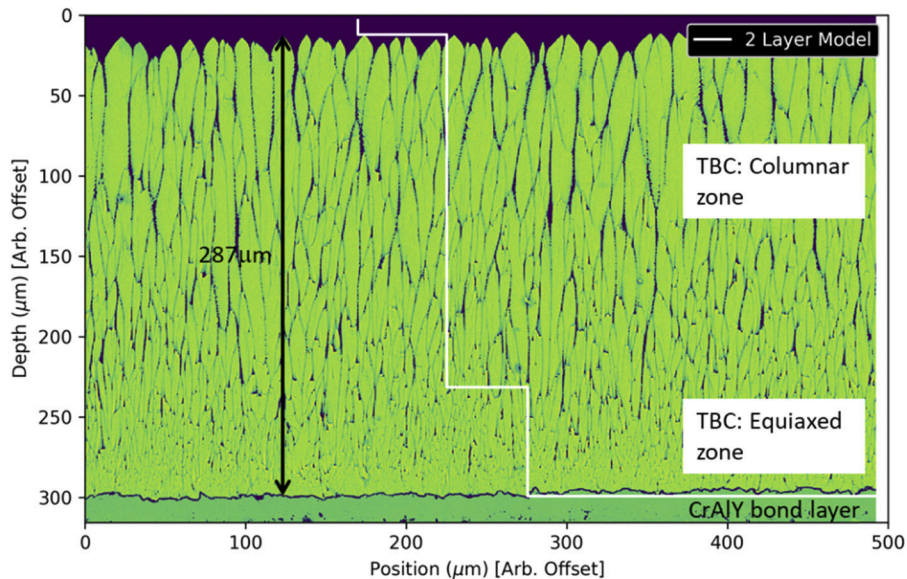

Fig. 9. Cross-section through center of YSZ-coated sample showing comparison with optical thickness fit over 1.25–1.35 THz frequency range.

In order to convert the optical thickness profile measured across the specimen to the physical thickness of the TBC, a coating refractive index of 3.977 was calculated using the n*t optical thickness (1141.3) and the SEM-measured coating thickness (287µm) at the center of the specimen. This value of refractive index was then used to convert the overall n*t optical thickness profile into a thickness profile to allow comparison to be made with the SEM-measured thicknesses, Fig. 10, for two orthogonal lines on the specimen. The specimen is longer in the y-direction and so the spherical thickness variation is larger than across the x-direction. The relative thicknesses of the columnar and equiaxed zones can be determined from the two-layer model fit, in which the relative thickness of the two layers was also adjusted as a fit parameter. The boundary between the two layers determined by the fit is shown in the cross-sectional SEM micrograph (Fig. 9). The THz beam diameter was approximately twice the SEM field-of-view and the value marked therefore represents spatial average across double the SEM field-of-view.

The specimen was cut parallel to the x-axis to produce cross-sections for the SEM measurements. Figure 10(a) shows the points measured from a single cross-section, while Fig. 10(b) represents
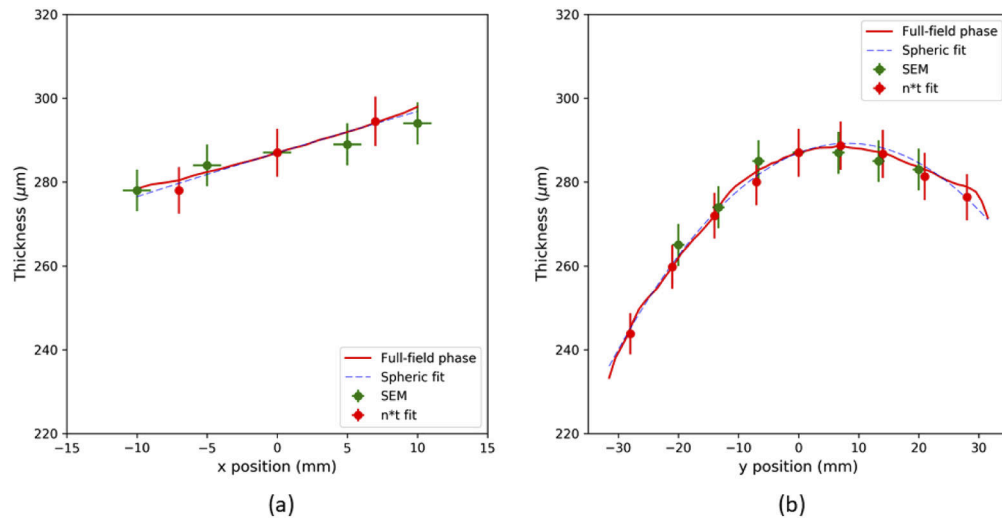
Fig. 10. Thickness measurements of YSZ-coated sample. (a) Variation with x-position across center of sample (b) Variation with y position down through center of sample.

the central value (at x=0) from seven separate cross-sections taken at different y-values. Each SEM cross-section required the dicing, mounting and polishing of the sample followed by the SEM measurement: this destructive and time-consuming procedure restricted the number of SEM data points. The n*t fit data points were recorded at 1mm x 1mm grid across the entirety of the sample and the error bars correspond to the 2% resolution mentioned previously.

5. Birefringence measurements

The retardation, and hence birefringence, of both the verification and thermal barrier coating samples was measured by rotating the sample in the x-y plane between two linear polarizers and recording the variation in reflected intensity as a function of rotation angle.

5.1. Verification sample

The retardation of the crystalline quartz wave plate, in the absence of dispersion in the birefringence, will vary linearly as the incident frequency is moved from the quarter-wave design frequency of 0.33 THz, with an expected retardation (modulo 2π) of 0 at 1.32 THz. This assumption was checked by measuring the variation in the reflected intensity as a function of sample angle at sixteen different frequencies across the frequency range 1.015–1.465 THz. This variation, described by Eq. (6), is shown for two different frequencies in Fig. 11 – the first, at 1.135 THz, with a theoretical retardation of 0.21 waves, and the second, at 1.315 THz, with a theoretical retardation of 0.004 waves.

The experimental retardation is calculated using Eq. (7) and compared with the retardation of the single layer thin-film model using the known material parameters. The variation with frequency of the thin-film model and its comparison with the experimental variation and the non-dispersive linear calculation are shown in Fig. 12. A simple linear model of the birefringence variation with frequency, neglecting the effect of the thin film nature of the sample, shows significant divergence from the measured birefringence. The inclusion of the thin film effects gives an almost identical trend in retardation although there is a non-zero offset in the experimental results.
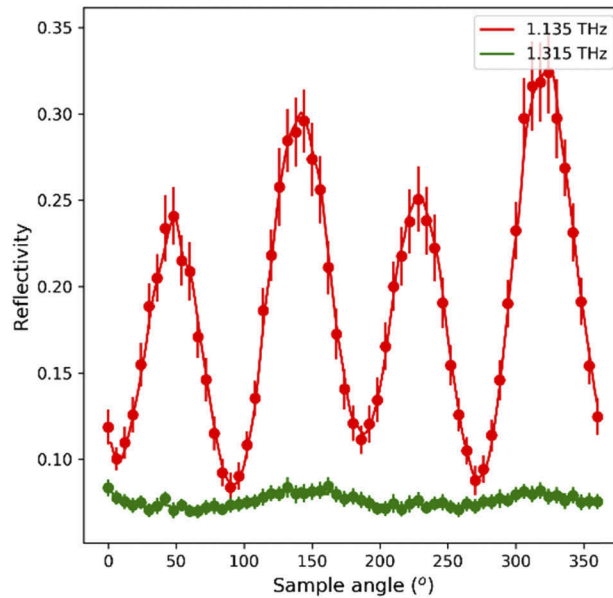
Fig. 11. Reflectivity variation with sample angle for GHz quarter-wave plate.
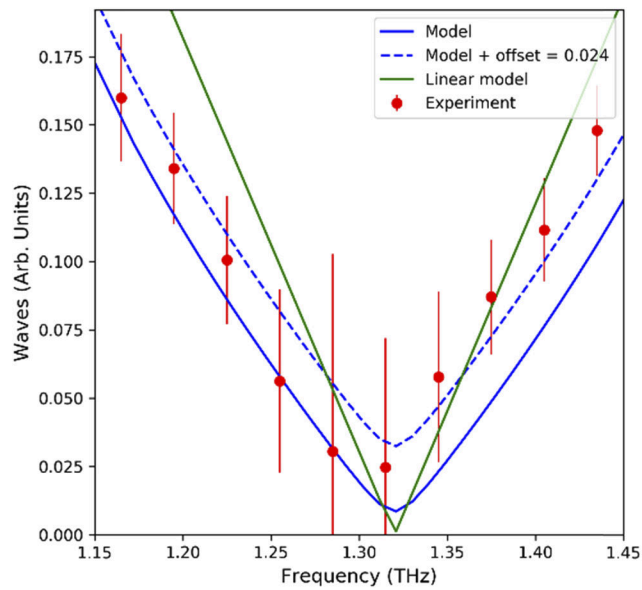

Fig. 12. Retardation of GHz quarter-wave plate showing thin-film model variation and comparison with experimental results (red) and simple linear calculation (green).

Potential sources of this birefringence offset are one (or more) of the optical elements (such as polarizers, beamsplitter, lenses etc.) in the beam path possessing some level of birefringence. The best match between the thin film model and the experimental results is attained when the offset is equal to 0.024 waves (i.e. approximately 10% of the maximum observed retardation).

5.2. Thermal barrier coating

The YSZ-coated sample used for the birefringence measurements was a specially designed sample with a flawed area at the center, where the β-NiAl bond coat was not applied prior to coating. This less-well bonded area is expected to exhibit a reduced level of stress compared to the area of the sample with the bond coat, due to the lower coupling strength between the substrate and the coating in the absence of the bond coat [26]. Figure 13(a) shows the measured birefringence variation along the vertical y-direction through the center of the YSZ-coated sample. It shows a local birefringence reduction in the area at the center of the sample without the bond coat. In addition, there is an increase in the birefringence towards the edges of the sample where edge-related stress concentration [27] occurs.
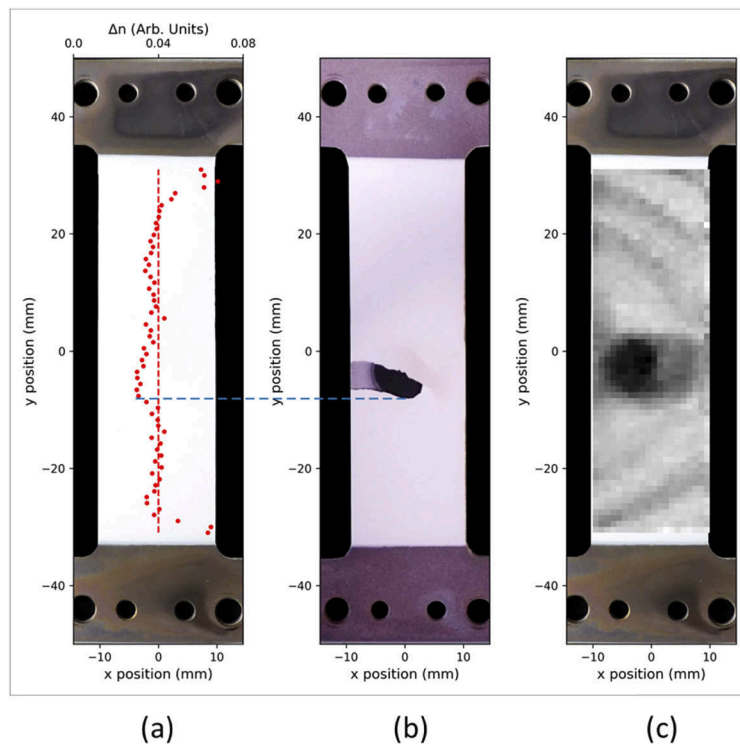

Fig. 13. (a) Birefringence of YSZ-coated sample (red) superimposed on white light image of sample immediately after fabrication. (b) White light image of failed coating after 30 h of accelerated thermal cycling. (c) Difference in unwrapped phase maps between 25 h and 0 h thermal cycling).

The sample was artificially aged by accelerated thermal cycling using a succession of 1 hour cycles to 1100 °C with forced air cooling, with both the THz optical thickness and birefringence measurements being performed after 20 and 25 hours. The coating failed after 30 hours of thermal cycling, Fig. 13(b), with the spallation site coinciding with the local variation in birefringence measured prior to aging. The image of the sample in Fig. 13(a) shows that the defect was not visible prior to aging. The optical thickness measurement showed a gradual increase during aging in the region of failure. Figure 13(c) shows the change in the full-field phase between the initial measurement at 0 hours and the measurement at 25 hours just prior to failure. This measurement indicates why it was sufficient to measure the optical thickness rather than refractive index or physical thickness, for our purposes.

6. Discussion

The preceding results have demonstrated an approach to measure thin film optical thickness and birefringence using a narrow linewidth THz source, with particular application to thermal barrier coatings. In general, the accuracy of the thickness measurement for the methods presented in this paper is in the 1-5% range, which is comparable to those reported for other THz measurement techniques, particularly for the TBC coatings and materials considered in this paper. The relatively high power of the THz source combined with the intensity normalization procedure for the reflectivity spectra enabled the measurements to be made without humidity control.

Results from the optical thickness verification samples, which were both structurally simpler and more consistent in their material properties than the TBCs, showed excellent agreement with the refractive index reported elsewhere in the literature. The refractive index of a TBC varies drastically depending on their quality and composition, even from coatings fabricated using the same equipment and processes [26–28], and a direct comparison with values in the literature is therefore not meaningful. The destructive sectioning of our TBC samples after optical measurement enabled us to confirm the agreement between the optical thickness estimate and the physical thickness measurement. In addition, the two-layer model was shown to give a good estimate of the sub-surface structure of the TBC.

The primary source of inaccuracy in the current system arises from the ∼10% pulse-to-pulse intensity variation of the THz laser system. This variation required each measurement point to be averaged over 50 pulses, giving a reasonable trade-off between measurement accuracy and speed. Dispersion in the THz samples also leads to some error, as observed in the discrepancy between the experimental data and the fitting results at the ends of the frequency range in Fig. 6(b). For small changes in the refractive index, such as those due to material dispersion in the THz range, any change in the frequency of the reflectivity minima is predominantly due to the δ_1 term in Eq. (4) rather than in the Fresnel reflections terms (ρ). The experimental and modelled fringe minima (indicated by the vertical dashed lines at frequencies f_{expt} and f_{model} in Fig. 6(b)) have the same optical phase (Eq. (1))

$$\delta = \frac{2\pi n_{expt}*t}{\lambda_{expt}} = \frac{2\pi n_{model}*t}{\lambda_{model}}$$

Substituting $n_{expt} = n_{model} + \Delta n$ & $\lambda_{expt} = \lambda_{model} + \Delta\lambda$ leads to a minimum peak wavelength shift of

$$\Delta\lambda = \frac{\lambda_{model}}{n*t}\Delta nt$$

where λ_{model} is the wavelength of the modelled minimum reflectivity point at the right hand end of Fig. 6(b) ($f_{model} = 1.373$ THz $\Rightarrow \lambda_{model} = 218.5$ μm), n*t is the optical thickness (= 1141.3 from the n*t fitting process) and t is the thickness of the sample (= 287μm from the physical sectioning measurements). The wavelength shift calculated from Fig. 6 is 1.8μm giving an estimated dispersion of dn/dλ=−0.00198, which compares well to the estimated TDS dispersion of dn/dλ ∼ −0.0019 [9] on a similar YSZ coated sample.

The birefringence measurements, which showed good agreement with theory for the verification sample, provides an alternative method of identifying potential flaws in the TBC structure immediately after manufacture and prior to going into service. The combination of the optical thickness and birefringence measurements indicated the point of failure of the deliberately flawed sample during accelerated thermal aging. An in-depth study of this combined approach will be reported in a future publication.

7. Conclusions

In this paper we introduced and verified a measurement technique, based on a narrow linewidth, tunable THz source, suitable for the measurement of the optical thickness and birefringence

of coatings that are opaque at visible wavelengths. The verification thickness measurements were within 1-4% of the values from the literature without the need for the environmental control. The optical thickness and birefringence of YSZ thermal barrier coatings were then measured, permitting additional verification of the optical thickness measurement method with SEM after destructive sectioning measurements of the sample. Finally, the combination of the two measurements was shown to suggest a way to predict likely points of failure during aging of the thermal barrier coatings.

Funding

Acknowledgements

Disclosures

The authors declare no conflicts of interest.

References

1. N. P. Padture, M. Gell, and E. H. Jordan, "Thermal Barrier Coatings for Gas-Turbine Engine Applications," Science **296**(5566), 280–284 (2002).
2. K. G. Kyprianidis, "Future Aero Engine Designs: An Evolving Vision," in *Advances in Gas Turbine Technology*, Ed. E. Benini, (IntechOpen, 2011)
3. H. M. Tawancy, N. Sridhar, N. M. Abbas, and D. S. Rickerby, "Failure mechanism of a thermal barrier coating system on a nickel-base alloy," J. Mater. Sci. **33**(3), 681–686 (1998).
4. Y. Ren, M. Pan, D. Chen, and W. Tian, "An Electromagnetic/Capacitive Composite Sensor for Testing of Thermal Barrier Coatings," Sensors **18**(5), 1630–1644 (2018).
5. Y. Ren, D. Chen, C. Wan, W. Tian, and M. Pan, "Calibration of micro-capacitance measurement system for thermal barrier coating testing," Rev. Sci. Instrum. **89**(6), 064703 (2018).
6. B. Jackson, "Terahertz Time-Domain Reflectometry of Multilayered Systems," Ph.D. Thesis, Univ. of Michigan (2008).
7. C.-C. Chen, D.-J. Lee, T. Pollock, and J. F. Whitaker, "Pulsed-terahertz reflectometry for health monitoring of ceramic thermal barrier coatings," Opt. Express **18**(4), 3477–3486 (2010).
8. D. J. Roth, L. M. Cosgriff, B. Harder, D. Zhu, and R. E. Martin, "Absolute Thickness Measurements on Coatings Without Prior Knowledge of Material Properties Using Terahertz Energy," NASA-TM 2013-216603 (2013).
9. T. Fukuchi, N. Fuse, T. Fujii, M. Okada, K. Fukunaga, and M. Mizuno, "Measurement of Topcoat Thickness of Thermal Barrier Coating for Gas Turbines Using Terahertz Waves," Elect. Eng. Jpn. **183**(4), 1–9 (2013).
10. D. Ye, W. Wang, J. Huang, X. Lu, and H. Zhou, "Nondestructive Interface Morphology Characterization of Thermal Barrier Coatings Using Terahertz Time-Domain Spectroscopy," Coatings **9**(2), 89 (2019).
11. J. Tennyson, P. F. Bernath, L. R. Brown, A. Campargue, A. Csaszar, L. Daumont, R. Gamache, J. T. Hodges, O. Naumenko, O. Polyansky, L. S. Rothman, A. C. Vandaele, and N. F. Zobov, "A database of water transitions from experiment and theory (IUPAC Technical Report)," Pure Appl. Chem. **86**(1), 71–83 (2014).
12. C. C. Katsidis and D. I. Siapkas, "General transfer-matrix method for optical multilayer systems with coherent, partially coherent, and incoherent interference," Appl. Opt. **41**(19), 3978–3987 (2002).
13. S. Krimi, G. Torosyan, and R. Beigang, "Advanced GPU-based terahertz approach for in-line multilayer thickness measurements," IEEE J. Sel. Top. Quantum Electron. **23**(4), 1–12 (2017).
14. J. Szczyrbowski, "Determination of optical constants of real thin films," J. Phys. D: Appl. Phys. **11**(4), 583–593 (1978).
15. P. Schemmel, G. Diederich, and A. J. Moore, "Measurement of direct strain optic coefficient of YSZ thermal barrier coatings at GHz frequencies," Opt. Express **25**(17), 19968–19980 (2017).
16. W. Wang, Z. Liang, C. Li, Y. Yin, and S. Wu, "Two-Intensity Measurement Method for Determining the Fast Axis and Phase Retardation of a Wave Plate," *2012 Symposium on Photonics and Optoelectronics*, Shanghai, 1–4, doi: 10.1109/SOPO.2012.6270565 (2012).
17. J. Singh, D. E. Wolfe, and J. Singh, "Architecture of thermal barrier coatings produced by electron beam physical vapor deposition (EB-PVD)," J. Mater. Sci. **37**(15), 3261–3267 (2002).
18. J. R. Nicholls, K. J. Lawson, A. Johnstone, and D. S. Rickerby, "Methods to reduce the thermal conductivity of EB-PVD TBCs," Surf. Coat. Technol. **151-152**, 383–391 (2002).

19. M. A. Ordal, R. J. Bell, R. W. Alexander, L. A. Newquist, and M. R. Querry, "Optical properties of Al, Fe, Ti, Ta, W, and Mo at submillimeter wavelengths," Appl. Opt. **27**(6), 1203–1209 (1988).

20. S. Kirkpatrick, C.-D. Gelatt Jr, and M. P. Vecchi, "Optimization by Simulated Annealing," Science **220**(4598), 671–680 (1983).

21. S. Kojima, H. Kitahara, S. Nishizawa, Y. S. Yang, and M. Wada Takeda, "Terahertz time-domain spectroscopy of low-energy excitations in glasses," J. Mol. Struct. **744-747**, 243–246 (2005).

22. M. Naftaly and R. E. Miles, "Terahertz time-domain spectroscopy of silicate glasses and the relationship to material properties," J. Appl. Phys. **102**(4), 043517 (2007).

23. A. D. Rakić, A. B. Djurišic, J. M. Elazar, and M. L. Majewski, "Optical properties of metallic films for vertical-cavity optoelectronic devices," Appl. Opt. **37**(22), 5271–5283 (1998).

24. M. Servin, J. A. Quiroga, and J. M. Padilla, "Fringe Pattern Analysis for Optical Metrology," (Wiley-VCH, 2014).

25. M. A. Herraez, D. R. Burton, M. J. Lalor, and M. A. Gdeisat, "Fast two-dimensional phase-unwrapping algorithm based on sorting by reliability following a noncontinuous path," Appl. Opt. **41**(35), 7437–7444 (2002).

26. Y. Chen, "Study of Bond Coats for Thermal Barrier Coating Applications," Ph.D. Thesis, Univ. of Manchester (2015).

27. K. Sfar, J. Aktaa, and D. Munz, "Numerical investigation of residual stress fields and crack behavior in TBC systems," Mater. Sci. Eng., A **333**(1-2), 351–360 (2002).

28. R. Darolia, "Thermal barrier coatings technology: critical review, progress update, remaining challenges and prospects," Int. Mater. Rev. **58**(6), 315–348 (2013).

Terahertz optical thickness and birefringence measurement for thermal barrier coating defect location

Waddie, Andrew J.